JOURNAL OF SYNCHROTRON RADIATION
ISSN 1600-5775

Methodological challenges of optical tweezers-based X-ray fluorescence imaging of biological model organisms at synchrotron facilities

Eva Vergucht,[a] Toon Brans,[b,c] Filip Beunis,[b,c] Jan Garrevoet,[a] Stephen Bauters,[a,d] Maarten De Rijcke,[e] David Deruytter,[e] Colin Janssen,[e] Christian Riekel,[d] Manfred Burghammer[d,a] and Laszlo Vincze[a]*

[a]Department of Analytical Chemistry, Ghent University, Krijgslaan 281, Ghent 9000, Belgium, [b]Department of Electronics and Information Systems, Ghent University, Sint-Pietersnieuwstraat 41, Ghent 9000, Belgium, [c]Center for Nano and Biophotonics, Ghent University, Sint-Pietersnieuwstraat 41, Ghent 9000, Belgium, [d]European Synchrotron Radiation Facility, 71 avenue des Martyrs, Grenoble 38000, France, and [e]Laboratory of Environmental Toxicology and Aquatic Ecology, Ghent University, Jozef Plateaustraat 22, Ghent 9000, Belgium.
*Correspondence e-mail: laszlo.vincze@ugent.be

Received 16 March 2015
Accepted 19 May 2015

Edited by P. A. Pianetta, SLAC National Accelerator Laboratory, USA

Keywords: X-ray fluorescence; optical tweezers; confocal XRF; single-cell imaging.

Supporting information: this article has supporting information at journals.iucr.org/s

Recently, a radically new synchrotron radiation-based elemental imaging approach for the analysis of biological model organisms and single cells in their natural *in vivo* state was introduced. The methodology combines optical tweezers (OT) technology for non-contact laser-based sample manipulation with synchrotron radiation confocal X-ray fluorescence (XRF) microimaging for the first time at ESRF-ID13. The optical manipulation possibilities and limitations of biological model organisms, the OT setup developments for XRF imaging and the confocal XRF-related challenges are reported. In general, the applicability of the OT-based setup is extended with the aim of introducing the OT XRF methodology in all research fields where highly sensitive *in vivo* multi-elemental analysis is of relevance at the (sub)micrometre spatial resolution level.

1. Introduction

Synchrotron radiation (SR)-based confocal X-ray fluorescence (XRF) imaging is attractive due to its multi-elemental non-destructive nature, high sensitivity and its potential of providing two- and three-dimensional information on the elemental composition of a variety of samples with trace-level detection limits (Vincze *et al.*, 2004; Šmit *et al.*, 2004, Kanngiesser *et al.*, 2003; Wilke *et al.*, 2010; De Samber *et al.*, 2010). When working with microscopic biological specimens in particular, SR-based imaging challenges involve the need to position and scan the sample while keeping it in its natural state as much as possible.

In 2011, Santucci *et al.* reported on a dedicated optical tweezers (OT) setup for SR microdiffraction experiments of micrometre-sized soft matter objects (*i.e.* starch and insulin crystals) in their natural aqueous environments at the ID13 Microfocus beamline of the European Synchrotron Radiation Facility (ESRF-ID13, France). Since then, we have further developed the compact OT setup and extended its application towards SR confocal XRF imaging of biological model organisms and single cells *in vivo* (Vergucht *et al.*, 2015). We recently reported the new OT XRF methodology combining optical tweezers technology for non-contact micro-sample manipulation with SR confocal XRF microimaging *for the first time*. The methodology allows for *in situ* elemental imaging of free-standing living cells in their aqueous environment

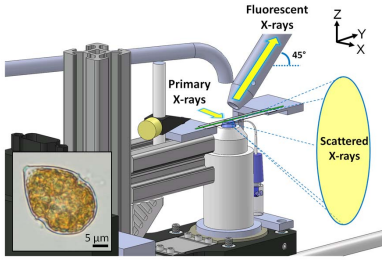

without the need for time-consuming and invasive sample preparation steps prior to analysis. Using the marine microalgae *Scrippsiella trochoidea* as a model organism [Figs. 1(*a*) and 1(*b*)], several successful test experiments focusing on applications in environmental toxicology have been performed at ESRF-ID13, demonstrating the feasibility, repeatability and high-throughput potential of the OT XRF methodology. Moreover, by combining the OT XRF methodology with complementary integrated small-angle X-ray scattering (SAXS) scanning techniques, it is possible to visualize the sample outline and internal sample structure, which also allows for the application of improved data processing strategies (Cojoc *et al.*, 2007, 2010). As demonstrated, sufficient submicrometre stability can be achieved by OT-based sample positioning for scanning X-ray analysis and X-ray-induced sample damage effects are expected to be significantly reduced by ultrafast scanning approaches (Vergucht *et al.*, 2015).

Yet, the integration and alignment of an optical tweezers setup at a synchrotron beamline are complex tasks that require careful optimization and trained experimentalists. Therefore, the current paper reports on the methodological challenges related to OT-based confocal imaging at synchrotron facilities, particularly at ESRF-ID13. The OT setup described here was originally designed for SR diffraction imaging of soft matter objects; therefore, we report on the OT setup developments necessary for XRF imaging, the optical manipulation possibilities and limitations of biological model organisms, and the associated challenges related to confocal XRF.

In general, we extended the applicability of the OT setup with the aim of introducing the OT XRF methodology in a number of research fields where highly sensitive *in vivo* multi-elemental analysis is of relevance at the (sub)micrometre spatial resolution level.

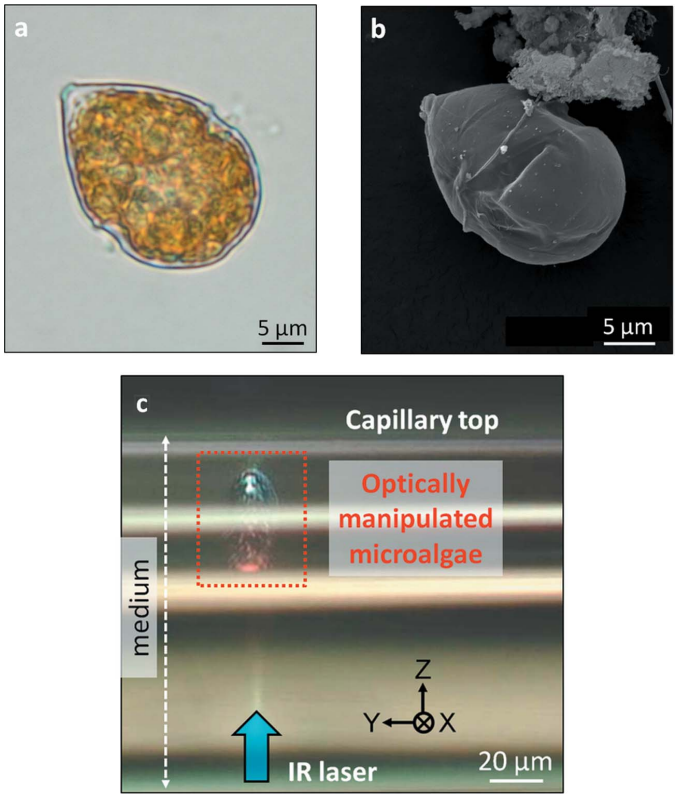

Figure 1
Scrippsiella trochoidea microalgae. (*a*) Microscopic image and (*b*) SEM image of a *S. trochoidea* algae. (*c*) Optically manipulated cell in aqueous medium. Microscopic image taken by the ESRF-ID13 Olympus beamline microscope.

2. Optical manipulation of biological model organisms: possibilities and limitations

As stated, the OT XRF methodology applies a laser-based optical tweezers setup as a revolutionary sample environment that enables non-contact sample manipulation and positioning of micrometre-sized biological specimens in their natural, aqueous environment. After its initial introduction by Ashkin in the early 1970s, the research field of optical tweezers has enjoyed a wide range of applications from atomic physics to medical science, thereby representing a focal point of interdisciplinary science (Lang & Block, 2003). OT-based applications are mainly situated within the research fields of molecular biochemistry and biophysics, allowing single molecule biophysical systems such as biopolymers (DNA), fractionated cells, molecular motors, *etc.* (Moffitt *et al.*, 2008; Appleyard *et al.*, 2007) to be investigated. Furthermore, optical tweezers can be applied purely as sample manipulators and positioning devices, which is the case for OT XRF imaging.

The physical principles of optical manipulation rely on the ability of light to exert pressure on dieletric matter (Maxwell, 1873). In particular, when directing a strongly focused laser beam onto a sample with a refractive index higher than compared with the surrounding medium, a pico-Newton restoring optical force will be established owing to the net momentum transfer from the scattering of incident photons. Depending on the sample size and the acting pico-Newton magnitude counterforces, optical manipulation is generally subdivided into optical trapping and optical levitation (Ashkin *et al.*, 1986; Ashkin & Dziedzic, 1971). Optical trapping phenomena take place below a certain size limit (several nm up to ~10 µm; Chu *et al.*, 1986) and one refers to optical levitation when a focused laser beam manipulation is employed on a slightly larger sample (10 µm to several tens of µm).

As we conducted research in the field of environmental toxicology, a large set of biological model organisms and standard reference materials were tested for their suitability towards optical manipulation. Critical parameters regarding the sample selection (*i.e.* organism/cell) for OT XRF imaging include optical and compositional properties, size, shape, mobility and toxicity, as discussed below.

Composition. When performing laser-based manipulation, the active optical force can be decomposed into two components: a gradient force and a scattering force. The gradient force is due to the steep laser intensity gradient caused by the

strongly focused laser and is directed along the spatial light gradient. The scattering force arises from the reflection and absorption of laser light and, therefore, compositional properties of the sample may enhance the laser light absorption effects, followed by sample temperature increase and unstable optical manipulation conditions. Supplementary Video 1 shows the attempts for optical manipulation of NIST SRM 2066 glass microspheres (~10 μm diameter) with a high iron content (~11% by weight). It can be seen that the Fe-rich microspheres reflect the directed laser light, most likely resulting in a strong scattering force in the direction of the incident light and no possibility for controlled optical manipulation. Note that this laser radiation-induced pressure effect can potentially be circumvented by trapping and handling a significantly absorbing sample in the centre of a Laguerre Gaussian beam profile, *i.e.* doughnut profile (Ashkin, 2006; Santucci *et al.*, 2012).

Size. Crucially, a balance should be made between the sample size and the amount of illuminated mass available for SR XRF analysis. Therefore, we focused on slightly larger biological model organisms and single cells with a size range of 20–40 μm; thereby, typically working within the optical levitation regime where gravitational counterforces pose an upper limit on the specimen size.

Shape. Concerning the sample shape, nonspherical optically manipulated specimens will align their longest dimension with the propagation axis of the laser beam, such that most of their volume is captured by the laser beam (Gauthier *et al.*, 1999). For example, fusiform-shaped diatoms (*e.g. Pseudo-nitzschia* sp.) will orient themselves vertically, *i.e.* along the laser beam. In the case of large and asymmetrically shaped biological organisms, multiple optical traps can be applied associated with an increase of the incident laser power.

Motility. Sample motility is another important parameter, because many biological organisms show adhesion behaviour or have the possibility to move around by means of flagella (long whip-like structures) or cilia (short). It has been shown that biological cells attached to a substrate can be optically levitated by applying a pulsed optical tweezers setup to overcome the binding interaction (Ambardekar & Li, 2005). Besides, adding chemicals to the medium can decrease/lower the motility, however potentially influencing the sample compositional and optical properties and resulting in poor trapping conditions.

Toxicity. As we found, microalgae represent a class of model organisms that generally comply well with the above-mentioned critical parameters. In particular, we selected the marine microalgae *Scrippsiella trochoidea* as a model organism (~35 μm width, Fig. 1) for optimizing the OT XRF methodology. This type of marine algae propels itself by means of two flagella and its motility is decreased by briefly washing the algal cultures in a HEPES buffer, imposing no effect on the optical manipulation properties. Regarding toxicity, *S. trochoidea* may form algal blooms and is, therefore, considered a harmful algae. Yet, while this species may produce some environmental effects such as hypoxia, this type of marine algae poses no threat to human health (Hallegraef *et al.*, 2003).

An optical microscope image of an optically levitated *S. trochoidea* microalgae in aqueous medium is shown in Fig. 1(*c*). The cell is contained within a horizontally mounted quartz capillary (QGCT 0.1, Capillary Tube Supplies Ltd, UK, 100 μm diameter, 10 μm wall thickness), optically levitated and translated to the upper capillary wall to prevent X-ray beam-induced vertical sample movement during a progressing scan (Vergucht *et al.*, 2015).

3. Optical tweezers-based XRF imaging

3.1. Compact OT setup

In general, an optical tweezers setup is composed of three essential components: a trapping laser, a high numerical aperture microscope objective (NA $\geq$ 1) and a sample observation system. A schematic CAD-representation and a block diagram of the OT setup and the corresponding laser path are shown in Fig. 2. The fibre laser represents the start of the optical path where a YLM-5-LP-SC ytterbium fibre laser

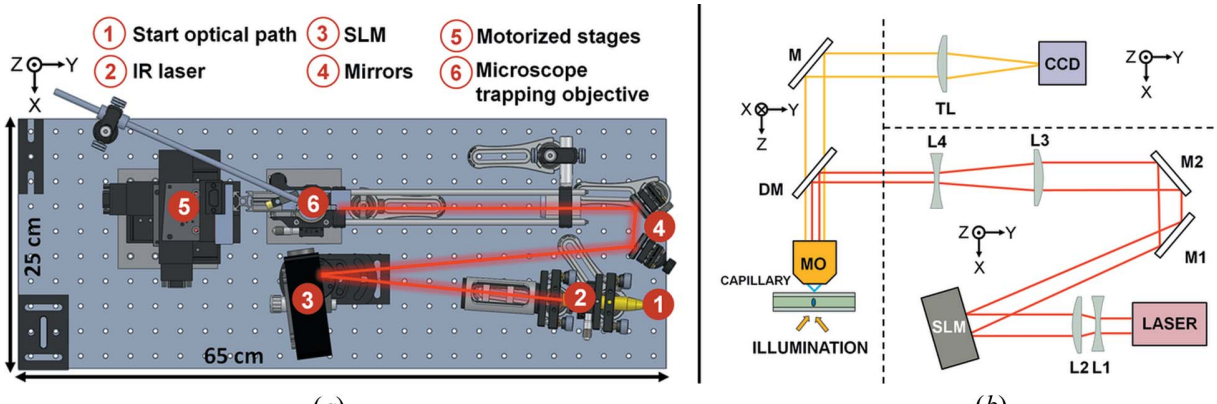

Figure 2
Overview of the OT setup. (*a*) CAD-drawing in SolidWorks and (*b*) block diagram of the OT setup with an indication of the IR laser path in red (L = lens, M = mirror, DM = dichroic mirror, MO = microscope objective, TL = tube lens). Note: all technical drawings are made in SolidWorks by the main author; the drawings of selected components were acquired from Thorlabs, Inc. (http://www.thorlabs.de).

source is applied (IPG Photonics, USA, class 4, 1070 nm) that delivers a TEM_{00} linearly polarized Gaussian beam. The near infrared output wavelength of 1070 nm is located in the window of relative transparency for biological materials and therefore induces negligible biological damage (Svoboda & Block, 1994; Neuman *et al.*, 1999). After beam expansion, the laser beam is directed onto a spatial light modulator (SLM; X10468-03 from Hamamatsu Photonics, Japan) that enables the creation of multiple optical traps *via* phase modulation. The latter is achieved by applying a certain voltage level to a layer of liquid crystals, without changing the incident intensity or the polarization state of the incident laser beam. Note that the SLM chip has a damage threshold of approximately 2 W and poses therefore an upper limit on the applicable laser power. After reflection onto several mirrors and passing through a set of lenses (operating in a 4F optical system), the laser beam is guided towards a water immersion microscope objective for focusing purposes (Olympus 100x LUMPlanFl, NA = 1). For aligning a cell to the trapping laser beam, the sample holder containing the biological specimen is translated by a set of *XYZ* motor stages (Micos MT-60). For sample observation, the sample is illuminated with a light guide and imaged onto a CCD camera by means of the same microscope objective and a tube lens. Note that the imaging system is located in a parallel plane below the optical laser path.

Owing to the spatial constraints often imposed by a synchrotron experimental hutch, the laser path alignment procedure is performed in a dedicated laser laboratory that provides sufficient spatial flexibility; thereby, using a second red laser (~650 nm wavelength, class 3B) which is available in the same laser unit. Right after the alignment procedure, the electric wiring is fixed firmly onto the optical breadboard, followed by the transport of the OT setup to the experimental hutch where the alignment is checked once again. Optical trapping of micrometre-sized polystyrene beads (Bangs Laboratories, Inc., 3.5 µm diameter) is then feasible if the OT setup is well aligned, as shown in Fig. S1 (supporting information). Note that due to the use of class 4 and class 3B laser beams, appropriate safety measures should be taken; wearing safety goggles with a sufficiently large optical density (*i.e.* 5–8, wavelength dependent) is mandatory, resulting in a safe level of transmitted fraction of laser photons towards the human eye.

3.2. OT XRF imaging at ESRF-ID13

For SR *in vivo* OT XRF imaging experiments, the compact OT setup is mounted on the beamline scanning stages of ESRF-ID13 and a raster scan is performed by translating the complete OT setup [Fig. 3(*a*), indication 1, Fig. S2]. Detection of the fluorescent photons is performed by a Vortex-EM energy-dispersive detector (50 mm^2 active area, 350 µm crystal thickness, 2 µs peaking time, Hitachi, USA) that is equipped with a polycapillary lens confocal optic (XOS, X-ray Optical Systems Inc., East Greenbush, New York, USA). The polycapillary detector lens defines a specific confocal micro-volume of detection that corresponds to the intersection

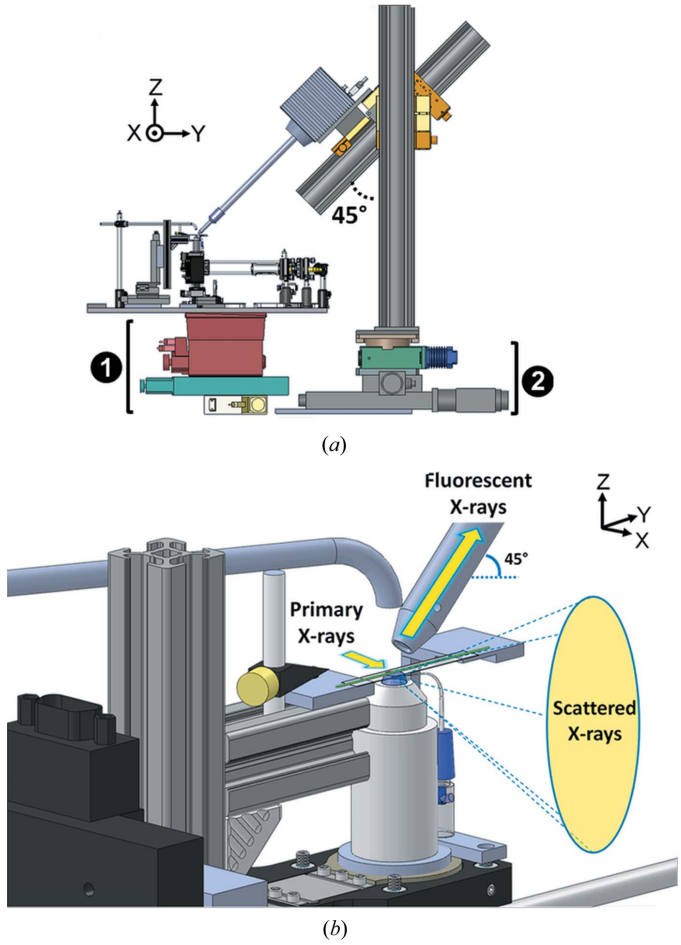

Figure 3
OT XRF technical overview. (*a*) Compact OT setup mounted on the beamline scanning stages (indication 1). The Vortex-EM detector is positioned under 45° with respect to the polarization plane, onto a set of translation stages (indication 2). (*b*) Detail of the sample area with an indication of the primary X-ray beam, confocal optic and the direction of the scattered photons.

volume of the primary X-ray beam and the energy-dependent acceptance of the polycapillary optic (Vincze *et al.*, 2004). Since only the XRF signal from the confocal micro-volume is detected (apart from secondary and higher order effects), a significant reduction of the interfering fluorescent/scatter signal from the surrounding sample environment (microscope objective, sample holder *etc.*) is obtained. Note that the Vortex-EM detector is tilted to an angle of 45° (with respect to the linear polarization plane) due to the geometrical constraints imposed by the short working distance of the confocal optic, thereby also reducing the absorption of the fluorescent signal by the sample capillary container. The fluorescence detector mount itself is positioned onto three translation stages used for confocal alignment purposes (Fig. 3*a*, indication 2). A schematic overview of the sample area (Fig. 3*b*) shows the direction of the primary X-ray beam and the confocal optic positioned under 45°. The instrumental preparation time prior to OT XRF imaging experiments requires approximately 24 h for integrating the OT setup in the beamline environment, including the offline OT setup

alignment, the transfer of the setup to the experimental hutch and the confocal XRF alignment procedure. Furthermore, sufficient time should be invested in the optimization of the scanning parameters, *i.e.* scanning step size, dwell time *etc.*

The scanning XRF data are complemented by SAXS patterns collected downstream by a MAXIPIX two-dimensional photon-counting X-ray detector (TAA22PC, 55 µm × 55 µm pixel size) and are used for sample outline and internal structure visualization (Ponchut *et al.*, 2011).

All OT XRF-associated devices are remotely controlled *via* SPEC commands, except for the CCD camera of the OT setup and the SLM which run on a Windows PC. Furthermore, a second Windows PC is installed in the experimental hutch for the initial alignment of the biological specimen to the IR laser; whilst the on-axis Olympus beamline microscope is applied for the alignment to the primary X-ray beam.

An overview of the combined OT XRF and integrated SAXS experimental results of a scanned *S. trochoidea* cell is shown in Fig. 4. The selected microalgae was cultured in an Ni-contaminated medium (50 µg l^{-1}, 48 h exposure), optically trapped and positioned to the upper capillary wall using a 0.5 W laser power throughout the confocal XRF scan. The cell was scanned using a 3 µm × 2 µm primary beam at a flux of approximately 3 × 10^{11} photons s^{-1} (2 µm step size, 0.2 s per point). Due to the relatively long exposure time, an extra beam stop was positioned in front of the MAXIPIX detector for protective purposes (Fig. S3), resulting in a significant reduction of the detected scattered signal. Consequently, a first data processing strategy involved identifying the number of illuminated pixels of each scattered pattern from which the outline of the scanned specimen can be clearly derived (Fig. 4*a*). Next, a threshold of the mean signal intensity and its standard deviation was set as a basis for the segmentation into algal outline and background regions (Fig. 4*b*). The algal region was subsequently projected onto the integrated SAXS distribution which is obtained by targeting a specific ROI that contains the strongest scattering intensity. After combining the isolated algae and the integrated SAXS distribution map, a subcellular structure is revealed that generated significantly more scattering signal (Fig. 4*c*).

Regarding the X-ray fluorescent signal, spectral deconvolution of the individual XRF spectra is performed by the nonlinear least-squares-fitting software *AXIL* (Vekemans *et al.*, 1994), followed by batch processing using the *MicroXRF2* software package written in IDL (Interactive Data Language; Exelis Visual Information Solutions, Boulder, CO, http://www.exelisvis.com). The intensity distributions of Mn, Fe and Zn derived from the scanned area [shown in Figs. 4(*d*)–4(*f*), respectively] display an accumulation centre which perfectly corresponds to the subcellular region obtained from the integrated SAXS pattern. These findings were confirmed by scanning multiple microalgae, demonstrating the complementary nature and potential of combining OT-based subcellular XRF imaging with integrated SAXS spectroscopy.

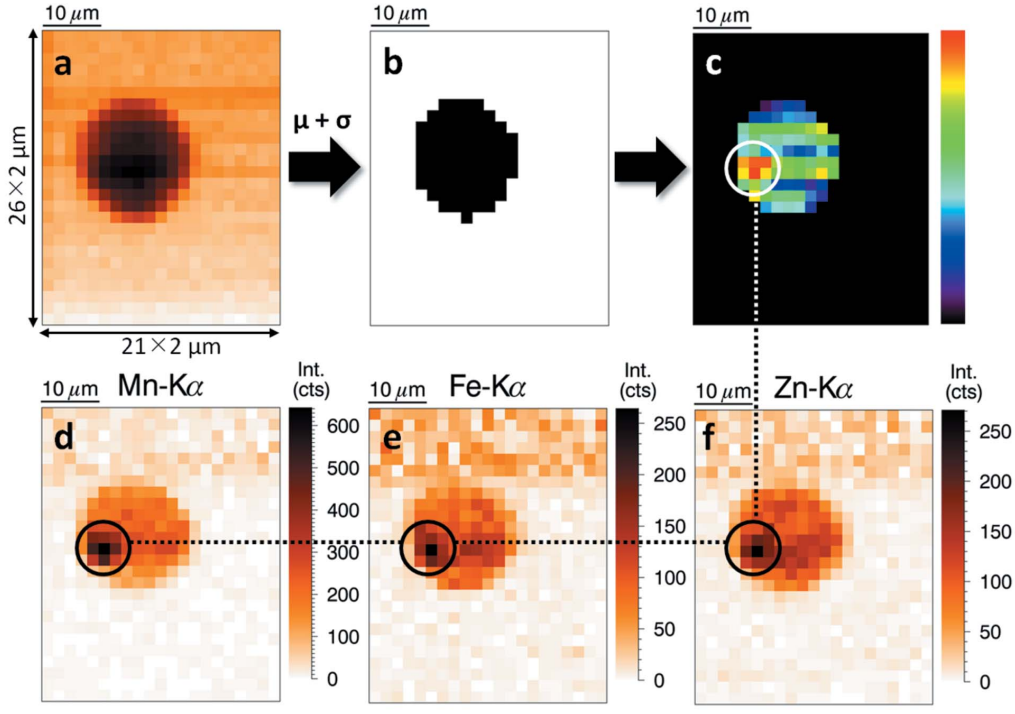

Figure 4
Combined XRF and integrated SAXS experimental results. (*a*) Scatter intensity map of a scanned algae based on the number of illuminated pixels from each scattering pattern (0.2 s exposure per point). (*b*) Algae isolated from (*a*) using $\mu + \sigma$ as a threshold. (*c*) Cell isolated from the integrated SAXS map based on (*b*). (*d*) Mn, (*e*) Fe and (*f*) Zn distribution maps of a scanned Ni-exposed algae with an indication of the accumulation centre (50 µg l^{-1} Ni, 48 h exposure).

Note that this accumulation centre most likely corresponds to an important organelle (*e.g.* nucleus, Golgi apparatus *etc.*); however, further experimental evidence is essential in this respect. Note that although the selected cell was cultured in a Ni-contaminated medium for 48 h, no significant Ni accumulation was observed, which corresponds to the findings described in our earlier work (Vergucht *et al.*, 2015).

4. OT setup developments for confocal XRF imaging

As mentioned earlier, Santucci *et al.* (2011) designed a dedicated OT setup for SR micro-XRD experiments of protein crystals in their natural environment and we extended its application to meet the experimental requirements of SR micro-XRF imaging. Here, we report on the main OT setup developments including the modifications to the optical breadboard, the start of the optical path, the droplet replenishment system and the sample holder.

4.1. Optical breadboard

For the OT XRF experiments in this study, the ESRF-ID13 beamline applied a transfocator focusing system incorporating a set of parabolic Be-refractive lenses providing a typical working distance of 10–25 cm (depending on the X-ray energy and the transfocator settings; Vaughan *et al.*, 2011), resulting in relaxed spatial constraints with respect to the OT setup. This spatial flexibility provides the possibility of using an optical breadboard with extended dimensions of 250 mm × 650 mm, oriented in the horizontal plane (Fig. S4*a*), providing sufficient spatial freedom for the polycapillary-based confocal (detector) optic. It should be noted that the relatively large optical breadboard results in an increase in weight of the total OT setup; thereby, potentially posing restrictions on the attainable scanning speed of the beamline stages. For future work, we propose a further miniaturization of the OT setup permitting it to be installed at even higher resolution nanofocus beamlines, which will also allow considerably faster scans with shorter exposure times due to its lower mass. Ultrafast scans with acquisition times in the (sub-)millisecond range per point (<50 ms pixel^{-1}) will also result in a significantly reduced influence of X-ray sample damage.

4.2. Laser optical path

The fibre laser represents the start of the optical path and should consequently be securely mounted by means of optomechanical components. The technical design in Fig. 5(*a*) shows that the laser beam collimator is held by a threaded adapter which is mounted onto a precision rotation mount (CRM1P, Thorlabs Inc.), both attached to a kinematic cage mount (KC1, Thorlabs Inc.) that can be tilted. In particular, the precision rotation mount can be fixed to a certain angle, which is a critical step in the IR laser polarization alignment. As mentioned, the fibre laser delivers a collimated, linearly polarized beam which should be aligned parallel to the orientation of the liquid crystals for optimal SLM functioning (Fig. 5*b*). After the laser collimator, a beam expander

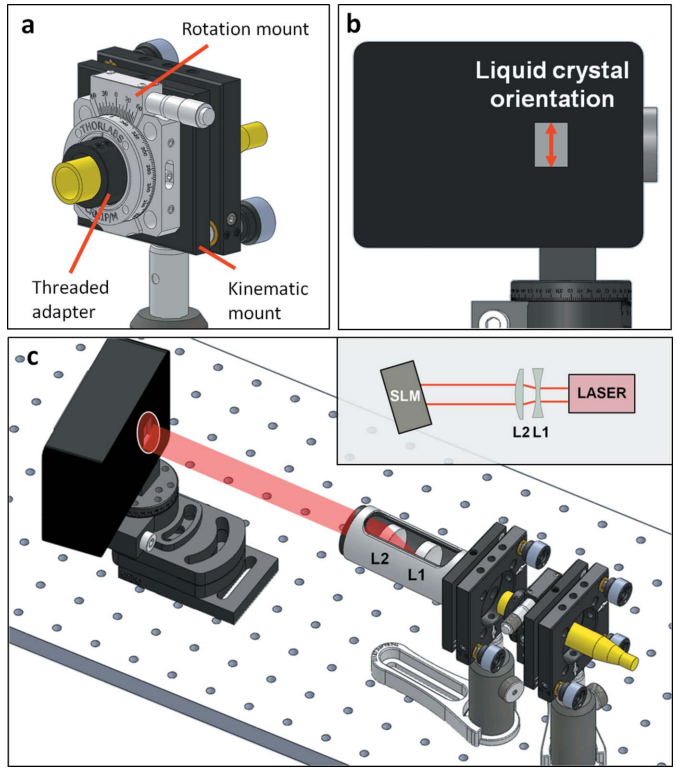

Figure 5
CAD-drawings of the start of the optical path. (*a*) Detail of the fibre laser mounting system (rotation mount colour was adapted). (*b*) Overview of the SLM with an indication of the liquid crystal orientation. (*c*) Overview of the laser beam expander tube.

consisting of a convex and a concave lens is inserted, resulting in a more complete illumination of the SLM chip (Fig. 5*c*). For our purpose, the SLM chip is positioned in upright geometry, which is beneficial for the reflection efficiency of mirrors M1 and M2 in vertical/ellipsoid geometry. Furthermore, the SLM positioning involves paying attention to the spatial freedom of the beamline camera and the MAXIPIX detector in view of diffraction experiments.

4.3. Droplet refill system

Compared with traditionally used oil immersion objectives, water immersion objectives have a slightly larger working distance (∼1 mm) and a closer match of the refractive index with the sample medium. However, as a water droplet on top of the objective is vital for proper focusing, compensation for water evaporation is essential. In view of this requirement, a droplet refill system was designed (Fig. 6) consisting of a bent needle (Sterican), an in-house made adapter piece and an ALADDIN2-220 (World Precision Instruments) syringe pump, providing a constant flow of ∼40 µl h^{-1} of Milli-Q water. Using this flow rate, the water droplet volume can be maintained at a constant level, permitting measurements for several hours without the need to enter the experimental hutch for water replenishment. The water flow rate, which depends on the intensity of the light guide/beamline micro-

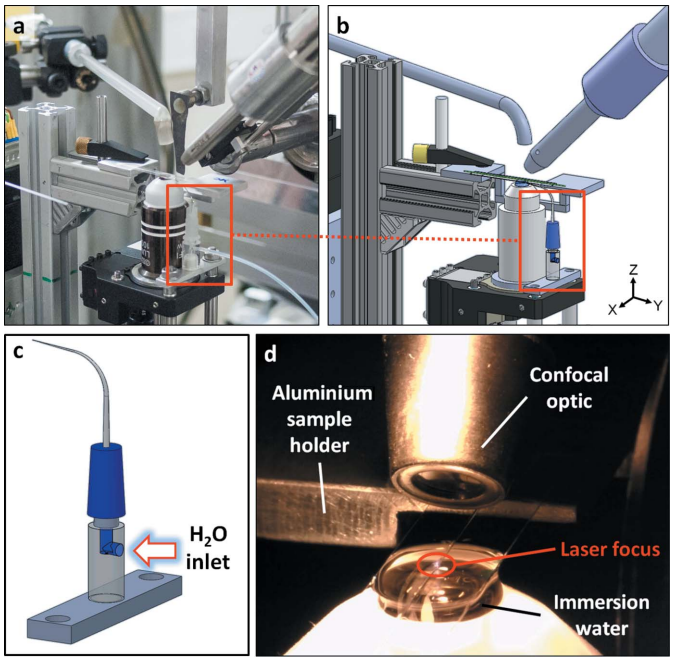

Figure 6
Water droplet refill system. (*a*) Photograph of the OT setup installed at ESRF-ID13 with an indication of the droplet refill system. (*b*, *c*) Corresponding CAD drawings. (*d*) Observation of the immersion droplet volume; photograph taken using a Dino-Lite digital microscope.

scope through thermal effects, is remotely adjusted *via LabVIEW* software (National Instruments); accompanied by visual observation using a Dino-Lite digital microscope (AD7013MTL Dino-Lite Premier).

4.4. Sample area

4.4.1. General outline. Owing to the geometrical requirements imposed by the detector confocal optic, a specific sample holder was designed for XRF imaging purposes, including a reversed bridging system and the partial extrusion of material [Figs. 7(*a*)–7(*c*) and 6(*d*)] to provide a large travel range in the positive *Y* direction. This sample holder is mounted perpendicularly to the primary beam and translated by means of *XYZ* motorized stages (Fig. 2*a*) integrated on the optical breadboard.

The microalgae and the medium are transferred by means of capillary forces into cylindrical quartz capillaries, which are open at both ends and afterwards sealed with putty to overcome evaporation of the medium. After a cleaning procedure using cotton swabs immersed in high-purity ethanol (ROTISOLV HPLC Gradient Grade, Carl Roth), the quartz capillary is positioned onto a thin quartz coverslip (UQG Optics Ltd, UV fused silica Spectrosil 2000, 40 mm × 5 mm × 0.10 mm thickness, L × W × H). The latter is subsequently mounted onto the aluminium holder which acts as a stable support. Finally, the mounted capillary is examined using a microscope and the coverslip is marked at positions with a suitable biological specimen, thereby, greatly facilitating the sample-to-laser beam alignment. For XRF imaging, all glassware in the vicinity of the trapping objective is composed of high-purity quartz to minimize spectral contributions. In particular, thin-walled cylindrical capillaries having 10 µm wall thickness are used as sample containers, in order to reduce the absorption of the emerging X-ray fluorescent signal on its way to the detector, as well as to eliminate/reduce the unwanted

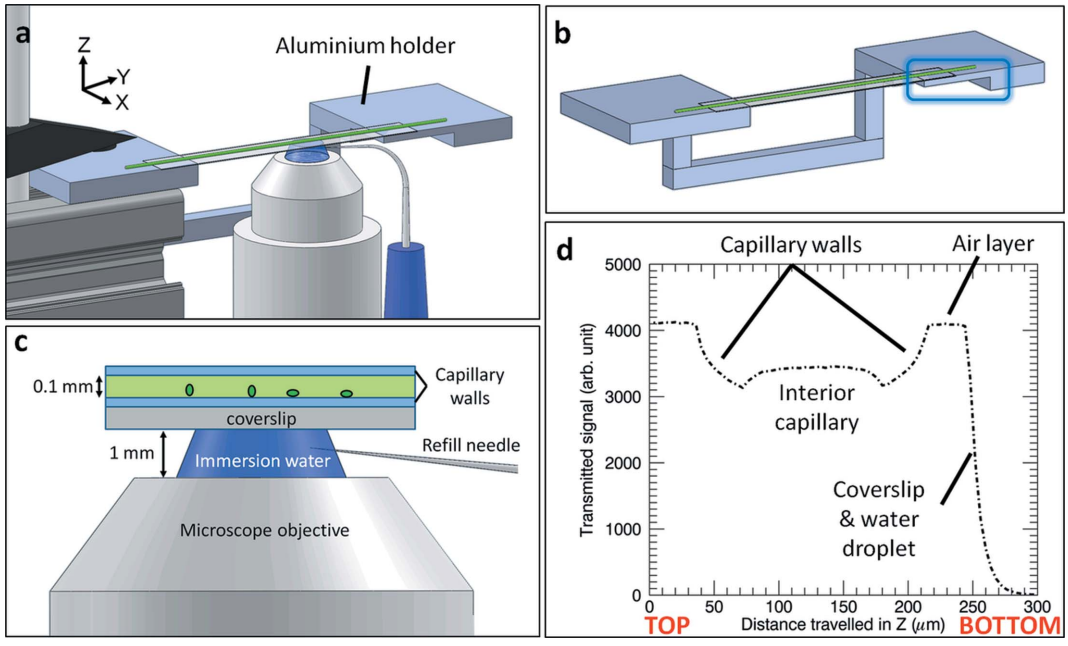

Figure 7
Sample area overview. (*a*) CAD representation of the mounted sample holder. (*b*) Aluminium sample holder with an indication of extruded material in blue. (*c*) Schematic design of the optical tweezers sample environment. The quartz capillary, filled with medium and microalgae, is mounted on top of a quartz coverslip. The dimensions are indicated by the double arrows and have a different scaling for clarity, adapted from Santucci *et al.* (2011). (*d*) Transmitted signal pattern by scanning a mounted sample through the X-ray beam.

contribution of spurious XRF signals from glass impurities and multiple scattering. Although the contribution of impurities from sample environment materials is strongly reduced by the confocal XRF detection principle, their influence through higher order interactions (*e.g.* second- and third-order fluorescence or scattering) cannot be fully eliminated, potentially resulting in reduced trace-element sensitivity.

By scanning a mounted sample in the vertical direction (Z) across the microbeam and detecting the transmitted beam intensity using a PIPS diode, one obtains very useful information on the sample alignment *via* the absorption properties of the sample container/mounting assembly. In Fig. 7(*d*), a decrease in transmitted intensity at both capillary walls is observed, with a clearly distinct low-absorbing region representing the capillary interior containing the algae and medium. Once the (relative) microbeam position is below the capillary, the transmitted signal increases due to the thin gap (layer of air) present between the capillary and the coverslip. Note that the thickness of this air layer should be minimized, typically reaching values between 10 and 30 µm, depending on the capillary mounting. In case the thickness of the layer of air exceeds a certain threshold, sample visualization by the beamline microscope will be reduced due to shadow effects, resulting in sample positioning difficulties combined with reduced optical manipulation capabilities. Finally, a steep signal decrease appears due to the absorption effects through the coverslip and the immersion water.

4.4.2. Objective coverslip and its implications. The application of a microscope objective coverslip (Fig. 7*c*) has several methodological implications. First, it allows on-axis sample observation while confining the immersion water droplet to the area below the capillary container. Without this spatial separation, the immersion water would surround the capillary, absorbing/refracting most of the visible light from the beamline microscope lighting, and hence inhibiting the alignment of a trapped sample (*i.e.* a single cell) to the primary X-ray beam. Due to this spatial confinement of the immersion medium, the coverslip also prevents the absorption of a large fraction of the incident and fluorescent X-ray photons by the immersion water. Next to this, the coverslip provides an efficient and fast way of checking the laser beam alignment for the optical trapping, as a concentric circular pattern should be observed in the case of proper laser alignment (Fig. S5*a*).

It should be noted, for the applied microscope objective, that in principle no coverslip should be applied, meaning that the optical manipulation actions should take place solely in the aqueous medium. The consequences of employing a coverslip involve distortions (mainly spherical aberrations) of the laser beam and consequently spreading out the laser focus in the axial direction. As we found, a sufficient gradient force is still established in the radial direction, capable of positioning a sample towards the point of highest laser intensity.

For X-ray scattering purposes, the coverslip absorbs a substantial amount of photons from the lower half of the scattering cone. The consequence of this second coverslip-related issue can be observed from the clear dividing line between coverslip and the sample at the dotted arrow in Fig. S5(*b*). A possible solution consists of considerably reducing the width of the coverslip ($\leq$1 mm).

5. Confocal XRF-related challenges

5.1. Initial attempts at conventional OT XRF imaging

While optimizing the OT XRF methodology at ESRF-ID13, initial attempts were made to perform conventional micro-XRF imaging by using only a simple detector collimator to limit the detector solid angle. Unfortunately, this approach resulted in the measurement of XRF spectra exhibiting overwhelming intensities of erroneous fluorescent and scattered signals, originating from the surrounding sample environment, including the microscope objective, coverslip *etc*. For example, Fig. 8(*a*) displays the Si and Zn fluorescent signal of a quartz capillary containing only seawater culture medium, which was scanned across the primary beam using conventional XRF detection (3 µm step size, 5 s dwell time per point). The Si signal originating from the quartz capillary shows a gradual decrease in function of the height due to self-absorption effects. Furthermore, two large Zn peaks indicate a contamination associated with the upper and lower wall of the

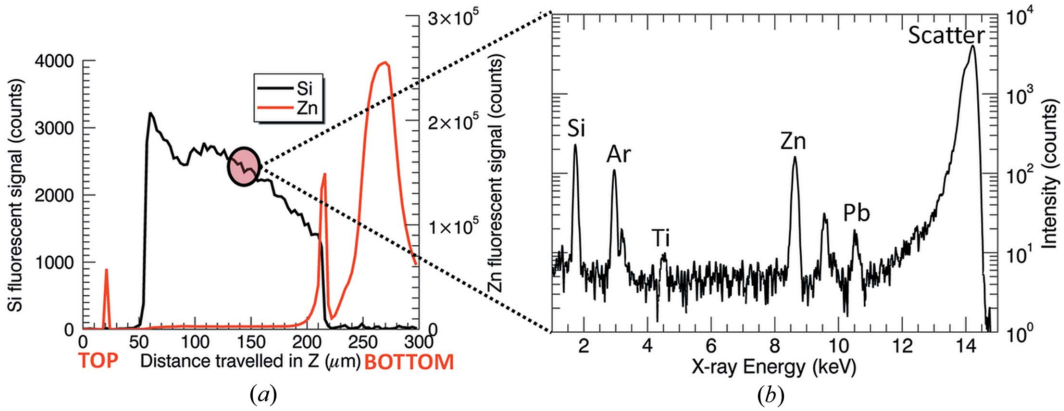

Figure 8
Conventional OT XRF imaging spectra. (*a*) Si and Zn fluorescent signals corresponding to a quartz capillary scanned across the X-ray beam (note that both *y* axes are differently scaled). (*b*) Single XRF spectrum from the interior of the capillary showing an intense Zn peak, most likely originating from the coverslip.

capillary tube, while the third intense Zn signal corresponds to a contribution of the coverslip, which in this measurement was composed of standard borosilicate glass with a considerable Zn content (Carl Roth, rectangular coverslips, No. 1871). In view of these observations, the sample preparation procedure was optimized: the quartz capillaries are now cleaned with high-purity ethanol to avoid contamination effects, the HEPES washing step lowers the background signal originating from the highly concentrated exposure medium and custom-made spectrochemically clean coverslips composed of high-purity quartz were purchased.

As shown in Fig. 8(*b*), the fluorescent spectrum from the capillary interior exhibits a large Zn fluorescent contribution as well, most likely originating from the coverslip as a result of secondary excitation, which causes strong interference in the case when Zn is the element of interest. These findings demonstrate the need to employ a confocal detection geometry where a polycapillary detector half lens defines a small micro-volume from which the XRF signal is detected, effectively cancelling out the XRF contribution from the sample environment.

5.2. Implications of the confocal working distance and confocal volume

For the OT XRF experiments performed in this study, the confocal optic is typically aligned to provide an acceptance path of approximately 50 µm (FWHM). This results in high transmission efficiency but poses limitations on the repeatability of the measurements. One potential issue involves the size of the selected microalgae (∼35 µm width), which is comparable to the dimensions of the confocal volume. Secondly, residual mobility of the algae can still manifest in the submicrometre range, even after the HEPES buffer treatment. Furthermore, both the beamline microscope and the confocal optic can become slightly misaligned or/and drift in the course of SR experiments. All of the above-mentioned factors can give rise to the alignment error depicted schematically in Fig. 9. In view of this potential problem, it is recommended to slightly defocus the confocal optic; thus increasing the working distance, resulting in a larger confocal acceptance (*e.g.* 100 µm, FWHM) and increased OT XRF repeatability. Note that a somewhat larger confocal volume will naturally generate a larger background in the XRF spectra, combined with a more intense Si fluorescent signal because a larger fraction of the capillary walls will overlap with the confocal detection volume.

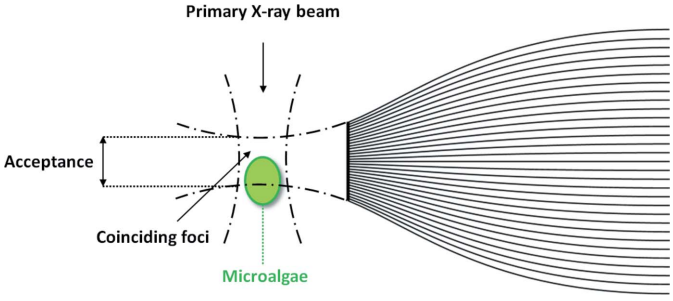

Figure 9
Schematic overview (top view) of the confocal detection geometry, illustrating potentially reduced OT XRF repeatability due to a too tightly aligned confocal volume with only a partial overlap with the cell of interest.

A slightly misaligned confocal volume can be noticed from the measured XRF spectra by examining the ratio of the XRF scatter peaks and targeting specific fluorescent signals. For instance, in the case when the polycapillary optic is focused on the capillary walls, the Rayleigh scattering contribution will strongly exceed the Compton peak when compared with the scattering ratio originating from the medium. Furthermore, the presence of Mn, Fe and Zn fluorescent peaks typically point towards the detection of the selected cell as shown in Figs. 4(*d*)–4(*f*). Therefore, it can be concluded that the absence of specific transition metals in the XRF spectra, particularly Mn, combined with the excessive presence of Si, typically indicate a slight confocal misalignment.

6. Conclusions and outlook

In this study, we reported on the possibilities and methodological challenges related to *in vivo* OT XRF imaging at synchrotron facilities, particularly at ESRF-ID13. We highlighted the critical parameters regarding the sample selection, the OT setup developments in view of XRF imaging and the confocal XRF-related challenges. Furthermore, the results of a recent ecotoxicological study at ESRF-ID13 were presented, demonstrating the subcellular complementary nature of OT-based XRF imaging combined with integrated SAXS measurements.

For future work, we propose a further miniaturization of the OT setup resulting in a decrease in weight and associated higher attainable scanning speeds of the beamline stages, thereby permitting the installation at higher resolution beamlines (Laforce *et al.*, 2014). In this respect, the attractive possibilities of innovative optofluidic lab-on-a-chip applications for particle manipulation and sensing can provide a powerful concept for miniaturization (Schmidt & Hawkins, 2011; Seo *et al.*, 2009). Furthermore, attempts will be made to optically manipulate more complex and nonhomogeneous biological model organisms *via* advanced *in situ* wavefront correction techniques using the SLM (Cizmar *et al.*, 2010). In addition, the SLM can shift optical traps to translate and rotate the sample, thereby making nanoscopic resolution motor stages redundant. The sample rotation made possible by the SLM even allows tomography experiments on microscopic samples with appropriate X-ray damage resistance, *i.e.* withstanding multiple passes over the same region.

In general, for future SR OT XRF experiments we propose a broad application range on a variety of microscopic (biological) samples that require *in vivo*, highly sensitive multi-element analysis with high spatial resolution. As a next step, we propose a cross-validation of the OT XRF results with those accessed *via* other highly sensitive chemical analyses at the (sub-)micrometre spatial resolution level. For instance, laser ablation inductively coupled plasma mass spectrometry is attractive due to its low limits of detection, capability of

providing isotopic information, and high sample throughput (Van Malderen *et al.,* 2015). Furthermore, X-ray fluorescence analysis of biological specimens under cryogenic vacuum conditions can provide information on the low atomic number elemental distributions, whilst minimizing sample radiation damage, which cannot be accessed by OT XRF due to absorption effects (Gerstel *et al.*, 2015). In spite of these advantages, both suggested methodologies require time-consuming, often invasive and error-prone sample preparation, which does not apply for OT XRF imaging, resulting in the attractive *in vivo* approach.

Acknowledgements

The authors wish to thank the staff of the ESRF-ID13 microfocus beamline, particularly B. Weinhausen and L. Lardiere, for their support prior to and during the synchrotron experiments. In particular, we acknowledge S. Santucci and D. Cojoc for their support regarding the OT setup development. The OT XRF measurements were performed in the framework of ESRF project Nos. EV-22, LS-2300 and EV-118, with additional financial support by the Funds for Scientific Research (FWO, Flanders, Belgium) contract No. G.0395.11 and Big Science program G.0C12.13 and the IAP-VI project photon@be funded by the Belgian Science Policy program (BELSPO). We thank Renaat Dasseville for the critical point drying sample preparation and the SEM analysis. E. Vergucht, T. Brans, J. Garrevoet and D. Deruytter acknowledge the Flemish Institute for the Promotion of Scientific and Technological Research in Industry (IWT, Flanders, Belgium) for their doctoral grant.

References

Ambardekar, A. A. & Li, Y. (2005). *Opt. Lett.* **30**, 1797–1799.
Appleyard, D. C., Vandermeulen, K. Y., Lee, H. & Lang, M. J. (2007). *Am. J. Phys.* **75**, 5–14.
Ashkin, A. (1971). *Appl. Phys. Lett.* **19**, 283–285.
Ashkin, A. (2006). *Optical Trapping and Manipulation of Neutral Particles Using Lasers.* Singapore: World Scientific Publishing.
Ashkin, A., Dziedzic, J. M., Bjorkholm, J. E. & Chu, S. (1986). *Opt. Lett.* **11**, 288–290.
Chu, S., Bjorkholm, J. E., Ashkin, A. & Cable, A. (1986). *Phys. Rev. Lett.* **57**, 314–317.
Cizmar, T., Mazilu, M. & Dholakia, K. (2010). *Nat. Photon.* **4**, 388–394.
Cojoc, D., Amenitsch, H., Ferrari, E., Santucci, S. C., Sartori, B., Rappolt, M., Marmiroli, B., Burghammer, M. & Riekel, C. (2010). *Appl. Phys. Lett.* **97**, 244101.
Cojoc, D., Ferrari, E., Garbin, V., Di Fabrizio, E., Amenitsch, H., Rappolt, M., Sartori, B., Laggner, P., Burghammer, M. & Riekel, C. (2007). *Appl. Phys. Lett.* **91**, 234107.
De Samber, B., Silversmit, G., De Schamphelaere, K., Evens, R., Schoonjans, T., Vekemans, B., Janssen, C., Masschaele, B., Van Hoorebeke, L., Szalóki, I., Vanhaecke, F., Rickers, K., Falkenberg, G. & Vincze, L. (2010). *J. Anal. At. Spectrom.* **25**, 544–553.
Gauthier, R. C., Ashman, M. & Grover, C. P. (1999). *Appl. Opt.* **38**, 4861–4869.
Gerstel, M., Deane, C. M. & Garman, E. F. (2015). *J. Synchrotron Rad.* **22**, 201–212.
Hallegraeff, G. M., Anderson, D. M. & Cembella, A. D. (2004). Editors. *Manual on Harmful Marine Algae.* UNESCO Publishing.
Kanngiesser, B., Malzer, W. & Reiche, I. (2003). *Nucl. Instrum. Methods Phys. Res. B*, **211**, 259–264.
Laforce, B., Schmitz, S., Vekemans, B., Rudloff, J., Garrevoet, J., Tucoulou, R., Brenker, F. E., Martínez-Criado, G. & Vincze, L. (2014). *Anal. Chem.* **86**, 12369–12374.
Lang, M. J. & Block, S. M. (2003). *Am. J. Phys.* **71**, 201–215.
Maxwell, J. C. (1873). *Treatise on Electricity and Magnetism.* Oxford: Clarendon Press.
Moffitt, J. R., Chemla, Y. R., Smith, S. B. & Bustamante, C. (2008). *Annu. Rev. Biochem.* **77**, 205–228.
Neuman, K. C., Chadd, E. H., Liou, G. F., Bergman, K. & Block, S. M. (1999). *Biophys. J.* **77**, 2856–2863.
Ponchut, C., Rigal, J. M., Clément, J., Papillon, E., Homs, A. & Petitdemange, S. (2011). *J. Instrum.* **6**, C01069.
Santucci, S. C., Amenitsch, H., Cojoc, D. & Riekel, C. (2012). *Synchrotron Radiation and Structural Proteomics*, edited by E. Pechkova & C. Riekel, pp. 183–212. Singapore: Pan Stanford Publishing.
Santucci, S. C., Cojoc, D., Amenitsch, H., Marmiroli, B., Sartori, B., Burghammer, M., Schoeder, S., DiCola, E., Reynolds, M. & Riekel, C. (2011). *Anal. Chem.* **83**, 4863–4870.
Schmidt, H. & Hawkins, A. R. (2011). *Nat. Photon.* **5**, 598–604.
Seo, S., Su, T. W., Tseng, D. K., Erlinger, A. & Ozcan, A. (2009). *Lab Chip*, **9**, 777–787.
Šmit, Z., Janssens, K., Proost, K. & Langus, I. (2004). *Nucl. Instrum. Methods Phys. Res. B*, **219–220**, 35–40.
Svoboda, K. & Block, S. M. (1994). *Annu. Rev. Biophys. Biomol. Struct.* **23**, 247–285.
Van Malderen, S. J. M., van Elteren, J. T. & Vanhaecke, F. (2015). *J. Anal. At. Spectrom.* **30**, 119–125.
Vaughan, G. B. M., Wright, J. P., Bytchkov, A., Rossat, M., Gleyzolle, H., Snigireva, I. & Snigirev, A. (2011). *J. Synchrotron Rad.* **18**, 125–133.
Vekemans, B., Janssens, K., Vincze, L., Adams, F. & Van Espen, P. (1994). *X-ray Spectrom.* **23**, 278–285.
Vergucht, E., Brans, T., Beunis, F., Garrevoet, J., De Rijcke, M., Bauters, S., Deruytter, D., Vandegehuchte, M., Van Nieuwenhove, I., Janssen, C., Burghammer, M. & Vincze, L. (2015). *Sci. Rep.* **5**, 9049.
Vincze, L., Vekemans, B., Brenker, F. E., Falkenberg, G., Rickers, K., Somogyi, A., Kersten, M. & Adams, F. (2004). *Anal. Chem.* **76**, 6786–6791.
Wilke, M., Appel, K., Vincze, L., Schmidt, C., Borchert, M. & Pascarelli, S. (2010). *J. Synchrotron Rad.* **17**, 669–675.